



Cite this: *Soft Matter*, 2024, 20, 6568

## Asymmetric toughening in the lap shear of metamaterial structural adhesives†

Chenghai Li,<sup>a</sup> Qiang Guo,<sup>a</sup> Robert Chambers<sup>b</sup> and Shengqiang Cai<sup>id</sup>\*<sup>ab</sup>

Metamaterial structural adhesives (MSAs), whose properties primarily rely on structural design, offer promising advantages over traditional adhesives, including asymmetric, switchable, and programmable adhesion. However, the effects of thick backing structures on the adhesion properties remain largely underexplored. Herein, we investigate a series of MSAs featuring a thin adhesive layer and an asymmetric thick beam structure terminated with a film. We conduct lap shear tests on the MSAs with varying terminated film thickness ( $t$ ) and beam tilting angle ( $\theta$ ) while maintaining an identical adhesive layer. For MSAs with a thick terminated film ( $t = 2$  mm), the effective adhesion energy is double that of solid samples without compromising shear strength, consistent with the theoretical predictions based on the crack trapping mechanism. Conversely, for MSAs with a thin terminated film ( $t = 0.5$  mm), the maximum shear strength and effective adhesion energy are  $\sim 2.8$  times and  $\sim 18.6$  times those of solid samples, respectively, deviating significantly from the theoretical predictions due to new crack initiations. We further explore adhesion asymmetry by tuning the beam tilting angle ( $\theta$ ). For MSAs with highly tilted beams ( $\theta = 70.3^\circ$ ), we achieve a maximum adhesion strength asymmetry factor of  $\tau_2/\tau_1 \sim 2.2$  for a thick terminated film ( $t = 2$  mm), and a maximum adhesion energy asymmetry factor of  $\Gamma_1/\Gamma_2 \sim 5.3$  for a thin terminated film ( $t = 0.5$  mm). Our work provides useful insights for designing metamaterial structural adhesives suitable for robotic grippers, wall-climbing robots, and wearable devices, particularly those requiring asymmetric, switchable, and stimuli-responsive adhesion, and adhesives on rough surfaces or in underwater conditions.

Received 8th April 2024,  
Accepted 5th August 2024

DOI: 10.1039/d4sm00410h

[rsc.li/soft-matter-journal](https://rsc.li/soft-matter-journal)

### 1. Introduction

Adhesives and tapes play crucial roles in various fields in modern society. Traditional adhesives and tapes largely rely on semi-empirical modification of bulk rheological properties and interfacial chemistry of polymers to achieve strong, tunable, or stimuli-responsive adhesion.<sup>1–8</sup> Achieving asymmetric adhesion is generally challenging through chemical modifications of bulk materials, which is strongly desired for emerging applications requiring switchable adhesion.<sup>6,7</sup> For example, for wearable devices, tissue adhesives, robotic grippers, and wall-climbing robotics, asymmetric adhesives can enable strong attachment in one direction during service and easy detachment in the other direction after service with reversibility.<sup>9,10</sup> Notably, metamaterial adhesives (MAs) have recently been explored, which have shown significantly enhanced adhesion, reversibility and reusability, directional and spatial programmability, universal adhesion to diverse substrates

without chemical modifications, and directionally asymmetric adhesion.<sup>9–21</sup> Representative examples of MAs include adhesive thin films with stiffness variations,<sup>11,20–23</sup> asymmetric adhesive thin films with nonuniform thickness profiles,<sup>17,24</sup> and kirigami-based adhesives with asymmetric cuts.<sup>9,10,14,25</sup> Previous MAs typically resemble thin pressure sensitive adhesives utilizing two-dimensional planar patterns, comprising a thin adhesive layer and a thin, mostly non-stretchable backing layer.

On the contrary, thick structural adhesives, *e.g.*, commercial foam tapes for insulating, protecting, and sound-dampening,<sup>26–28</sup> are typically composed of a thin adhesive layer and a relatively thick and compliant backing structure. In recent years, new structural adhesives have been developed, exhibiting some unique benefits for engineering applications in robotic grippers<sup>15,16,29</sup> and wall-climbing robots.<sup>30,31</sup> For example, a recent study presented a structural adhesive utilizing bistable beams within an enclosed frame as the backing, together with an adhesive tape for pick-and-release purposes.<sup>16</sup> Another study proposed a structural adhesive for robotic grippers employing a thick backing structure composed of periodic, tilted beams and a gecko-inspired adhesive layer for enhanced grasping.<sup>15</sup> Notably, an earlier study demonstrated that a hollow backing with symmetric vertical beams could significantly enhance the adhesion energy of gecko-inspired structural adhesives through crack trapping-induced adhesion

<sup>a</sup> Department of Mechanical and Aerospace Engineering, University of California, San Diego, La Jolla, CA 92093, USA. E-mail: [s3cai@ucsd.edu](mailto:s3cai@ucsd.edu)

<sup>b</sup> Materials Science and Engineering Program, University of California, San Diego, La Jolla, CA 92093, USA

† Electronic supplementary information (ESI) available. See DOI: <https://doi.org/10.1039/d4sm00410h>

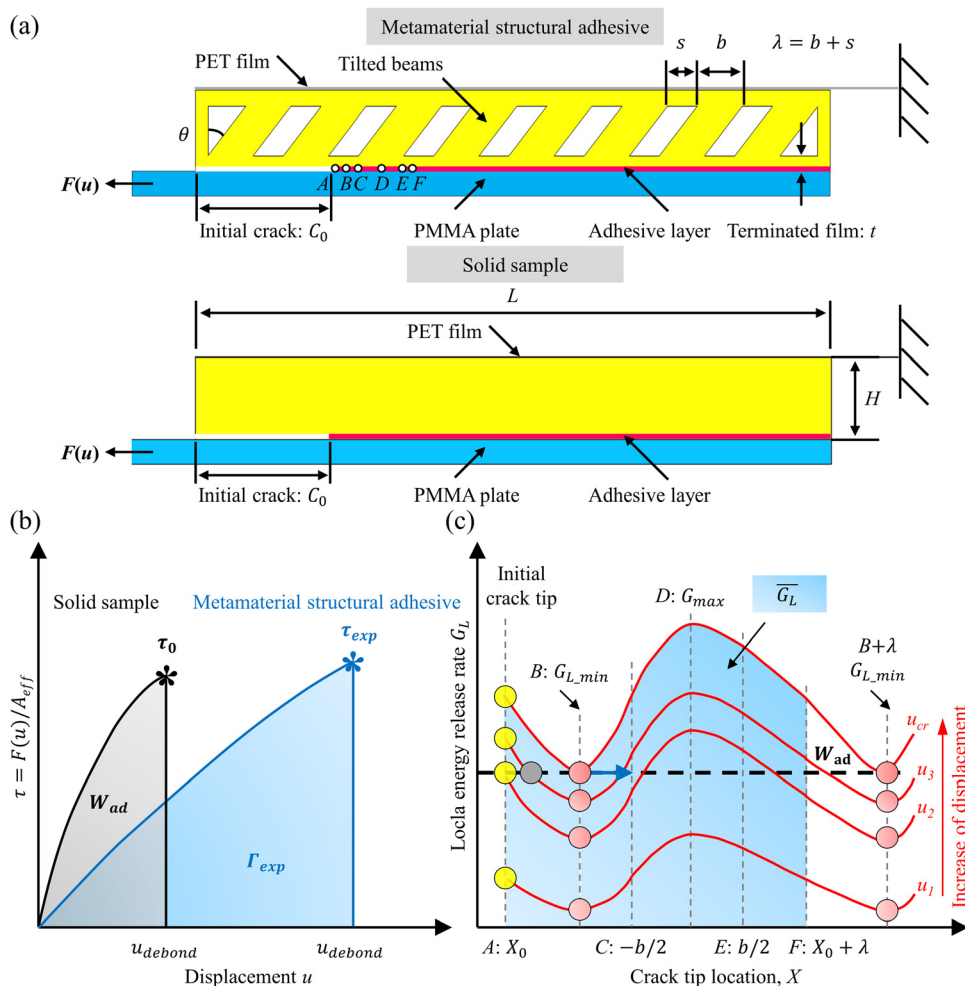


**Fig. 1** Adhesion toughening arising from the crack trapping mechanism in the lap shear of metamaterial structural adhesives. (a) Schematics depicting lap shear tests for both the hollow MSA (top) and solid sample (bottom), with labeled geometric dimensions and horizontal positions. (b) Representative shear stress–displacement curves for the MSA (blue) and solid sample (black), respectively. For the solid sample, the black star symbol indicates the intrinsic shear strength  $\tau_0$  and the shaded area represents the intrinsic work of adhesion  $W_{ad}$ . For the MSA, the blue star symbol indicates shear strength  $\tau_{exp}$  and the shaded area indicates the effective adhesion energy  $\Gamma_{exp}$ . (c) Local energy release rate  $G_L$  around the crack tip versus the crack tip location  $X$  for the MSA (red lines). The black dashed line represents  $W_{ad}$ . Yellow circles denote  $G_L$  at the initial crack tip ( $X = X_0$ ). Red circles denote the minimum of  $G_L$  at  $X = X_{min}$  and  $X = X_{min} + \lambda$ . With the increase of the applied shear displacement  $u$ ,  $G_{L,min} = W_{ad}$  is satisfied at the critical displacement ( $u = u_{cr}$ ), leading to unstable crack propagation (blue arrow). The blue shaded area, divided by the period  $\lambda$ , represents the averaged energy release rate  $\overline{G_L}$ . Note that the relationship between local energy release rate and crack length depends on the geometric parameters of the hollow backing structures, as reported in a previous theoretical study.<sup>33</sup>

toughening.<sup>13</sup> Another study measured asymmetric adhesion using indentation tests and frictional properties using sliding tests of gecko-inspired structural adhesives with an asymmetric, hollow backing structure consisting of periodic tilted beams.<sup>32</sup> However, the mechanistic understanding and quantitative influence of asymmetric backing structures on adhesion toughening and asymmetry of thick structural adhesives under shear loading remains unexplored in fracture-dominated conditions.

In this study, we develop a series of metamaterial structural adhesives (MSAs) comprising two components: a thin adhesive layer and a thick and asymmetric hollow backing consisting of tilted beams terminated with a film (Fig. 1a, top). The hollow structure was originally designed as the backing of the structural adhesive for robotic grippers, as reported in a previous

study.<sup>15</sup> Subjected to an external shear force, the hollow backing undergoes beam buckling, allowing different structural adhesives, *i.e.*, adhesive pads of the robotic grippers, to equally share the load. In our study, we aim to combine experimental, numerical, and theoretical methods to study how the geometry of the backing structure affects the adhesion properties of MSAs under lap shear tests in fracture-dominated conditions. We conduct lap shear tests using one rigid PMMA plate and one flexible PET film (Fig. 1a).

Our results have shown that for MSAs with a relatively thick terminated film ( $t = 2$  mm), the effective adhesion energy is approximately twice that of solid samples, without compromising their shear strength. Our theoretical and numerical analyses identify crack trapping as the toughening mechanism if

the crack propagates unidirectionally following a predefined path. For hollow MSAs, with a fixed shear displacement, the energy release rate varies periodically with the crack length, causing unstable crack propagation in practical loadings and thus adhesion toughening. For MSAs with a relatively thin terminated film ( $t = 0.5$  mm), the maximum shear strength is  $\sim 2.8$  times and  $\sim 2.4$  times that of solid samples for two opposite pulling directions, and the effective adhesion energy is  $\sim 18.6$  times and  $9.8$  times that of solid samples for two opposite pulling directions. However, new crack initiation at the interface may lead to a substantial deviation between experimental results and theoretical predictions based on the crack trapping mechanism. Furthermore, we explore the adhesion asymmetry by varying the beam tilting angle  $\theta$ . For MSAs with a thick terminated film ( $t = 2$  mm), a shear strength asymmetry factor of  $\tau_2/\tau_1 \sim 2.2$  is achieved for highly tilted beams ( $\theta = 70.3^\circ$ ), while the adhesion energy asymmetry factor  $\Gamma_2/\Gamma_1$  is less dependent on  $\theta$  due to the crack trapping mechanism for both pulling directions. For MSAs with a thin terminated film ( $t = 0.5$  mm), a strength asymmetry factor of  $\tau_1/\tau_2 \sim 1.4$  and an adhesion energy asymmetry factor of  $\Gamma_1/\Gamma_2 \sim 5.3$  are attained for highly tilted beams ( $\theta = 70.3^\circ$ ). Our research may provide useful insights to develop metamaterial structural adhesives with enhanced, asymmetric, and switchable properties through simple structural designs.

## 2. Experimental methods

### 2.1 Fabrication of the MSAs

To fabricate the thick backing structures with relatively thick terminated films ( $t = 1, 1.5$  and  $2$  mm) (Fig. S1a, ESI<sup>†</sup>), we first printed a rigid mold with the fused filament fabrication printer (FlashForge Guider 2) or the high-resolution polyjet printer (Connex 3 Objet 500, Stratasys). Then, we mixed parts A and B of Dragon Skin 00-30 (Smooth-on) in a 1:1 weight ratio. The precursor underwent mixing using the ARM-310 mixer (THINKY) at 2000 RPM for 1 min, followed by refrigeration for 5 min, and a final mixing step at 2000 rpm for 1 min. The resulting precursor was poured into the mold and left at room temperature for 4 h for curing.

To fabricate the thick backing structures with relatively thin terminated films ( $t = 0.5$  or  $0.75$  mm) (Fig. S1b, ESI<sup>†</sup>), we first followed the above procedures to fabricate one part of the hollow structure. We then injected the Dragon Skin precursor into a sandwiched mold with a silicone spacer ( $t = 0.5$  or  $0.75$  mm) to fabricate the thin terminated film. Next, we mixed the base and curing agent of PDMS (Sylgard 184, Dow Corning) at a 20:1 weight ratio, and then added a Pt-catalyst (Gelest SIP6831.2) at  $0.5 \mu\text{L g}^{-1}$ . The PDMS precursor was mixed for 2 min and degassed for 5 min in a vacuum pump, which was then used to bond the thin terminated film with the molded partial hollow structure. We stored the assembled sample in a  $60^\circ\text{C}$  oven overnight for curing.

We listed the dimensions of hollow structures in Fig. S1c and Table S1 (ESI<sup>†</sup>). The length, height, and width of the hollow backing structure are denoted as  $L$ ,  $H$ , and  $w$ , respectively.

The beam tilting angle is denoted as  $\theta$ . The width of a beam and the spacing between two neighboring beams are denoted as  $b$  and  $s$ , respectively. The spatial period of the hollow structure is thus  $\lambda = b + s$ . The number of periods/beams is denoted as  $N$ . The thickness of the terminated film is denoted as  $t$ . For each backing design, we fabricated the solid sample with the same dimensions of  $L \times H \times w$  to measure the intrinsic adhesion properties.

We next bonded a polyethylene terephthalate (PET) thin film ( $75 \mu\text{m}$ , McMaster Carr) to the top of the backing structure using the silicone adhesive (Loctite 908570). Then, we mixed the base and curing agent of PDMS at a 15:1 weight ratio and added the Pt-catalyst (Gelest SIP6831.2) at  $0.5 \mu\text{L g}^{-1}$ . We used the PDMS precursor to bond the backing structure to a rigid polymethyl methacrylate (PMMA) plate (3 mm). We stored the assembled sample at room temperature overnight and then in a  $50^\circ\text{C}$  oven for curing. The fabricated MSAs had an ultra-thin PDMS adhesive layer ( $t \sim 0.08$  mm) with the shear modulus ( $\mu$ ) of  $0.3 \text{ MPa}$ <sup>34</sup> (Fig. 1a). Notably, both PET film and PMMA plate matched the width of the hollow backing. We prepared the solid samples using identical procedures (Fig. 1a).

### 2.2 Lap shear tests of MSAs

As shown in Fig. 1a, we introduced an initial crack with the length of  $C_0$  (Table S1, ESI<sup>†</sup>) at the interface between the PDMS adhesive layer and the PMMA plate. Then, we tested all samples using a tensile machine (5965 Dual Column Testing Systems; Instron) equipped with a 1 kN load cell. We fixed the ends of the PET film and PMMA plate to the bottom and top grippers, respectively. Then, we applied monotonic loading to all the samples at a rate of  $0.05 \text{ mm s}^{-1}$  until the MSAs completely debonded from the PMMA plate. Simultaneously, we recorded force–displacement curves and filmed all the tests with a digital camera (Canon 60D). In all tests, adhesive failure was consistently observed between the PDMS adhesive layer and the PMMA plate, rather than debonding between the PDMS adhesive layer and the hollow backing structure (Fig. 2b).

We measured the intrinsic adhesion properties from solid samples. The intrinsic shear strength ( $\tau_0$ ) is defined as the maximum force ( $F_{\text{max}}$ ) divided by the effective adhesion area ( $A_{\text{eff}}$ ), *i.e.*,  $\tau_0 = F_{\text{max}}/A_{\text{eff}}$ , where  $A_{\text{eff}} = (L - C_0) \times w$ . The intrinsic work of adhesion ( $W_{\text{ad}}$ ) is defined as the input work to rupture the entire interface divided by  $A_{\text{eff}}$ , *i.e.*,  $W_{\text{ad}} = \frac{1}{A_{\text{eff}}} \int_{u=0}^{u=u_{\text{debond}}} F du$ , where  $u_{\text{debond}}$  is the displacement at which the force drops to zero.

Similarly, for MSAs, we define the shear strength ( $\tau_i$ ) and the effective adhesion energy ( $\Gamma_i$ ) as  $\tau_i = F_{i,\text{max}}/A_{\text{eff}}$  and  $\Gamma_i = \frac{1}{A_{\text{eff}}} \int_{u=0}^{u=u_{\text{debond}}} F du$ , respectively, where  $i = 1$  or  $2$  represents the two opposite pulling directions. The normalized shear strength and normalized adhesion energy of MSAs relative to solid samples are defined as  $\tau_i/\tau_0$  and  $\Gamma_i/W_{\text{ad}}$ , respectively.

### 2.3 Finite element simulation

We simulated the lap shear tests of MSAs in Abaqus using a static, general method. We adopted linear elastic models for

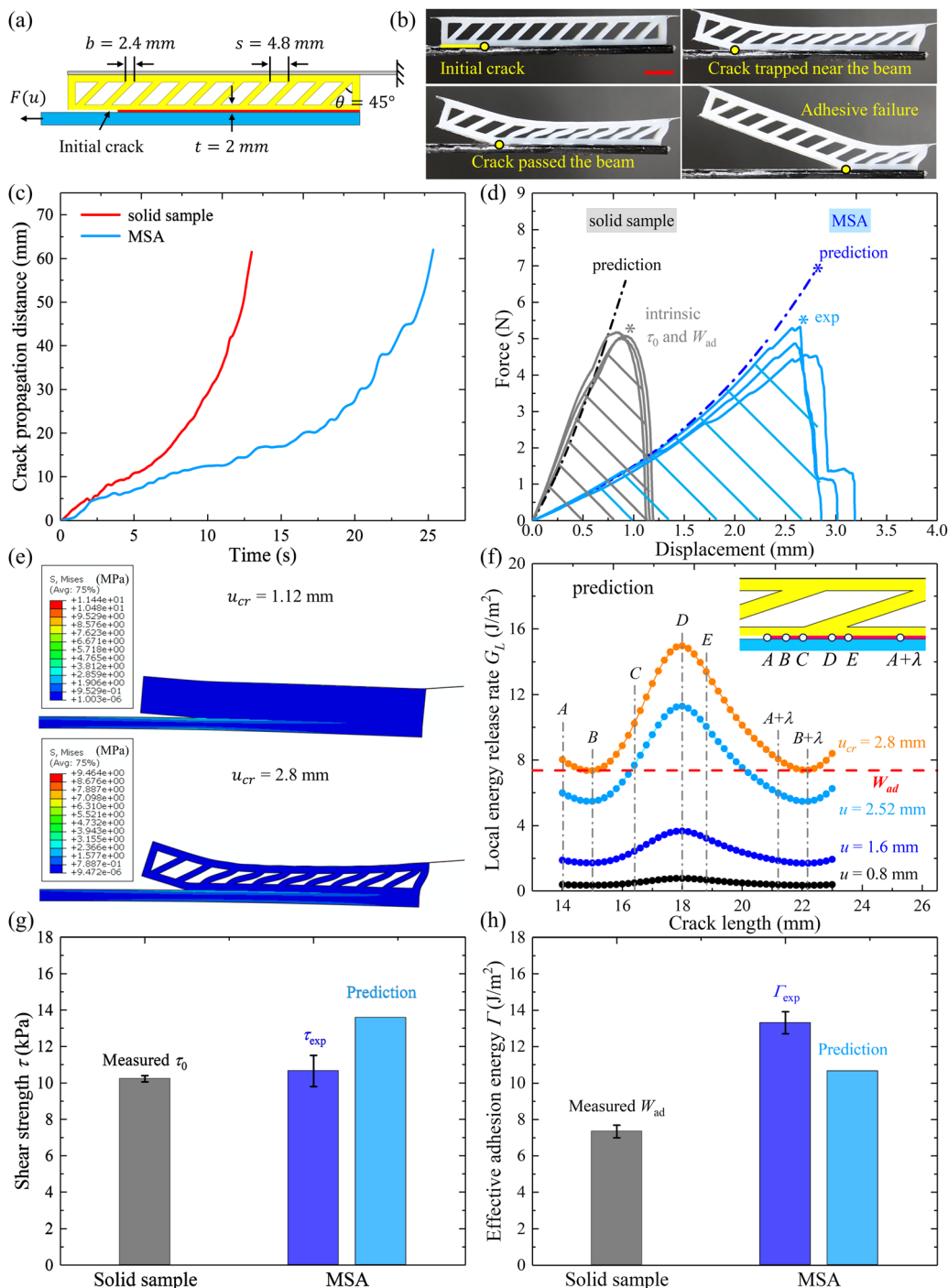


**Fig. 2** Agreement between experimental measurements and MSA and theoretical predictions in the lap shear of MSAs with slender beams and a thick terminated film when the crack propagates unidirectionally along the predefined path. (a) Schematic showing the lap shear test and the geometric parameters of the MSA. (b) Images capturing the crack propagation dynamics, with the crack tip highlighted by a yellow circle. Scale bar, 1 cm. (c) Crack propagation distance versus time for both the solid sample and the MSA. (d) Comparison between experimental and predicted force–displacement curves for the solid sample and the MSA, respectively. Predicted curves are truncated at  $u = u_{cr}$  where  $G_{L\_min} = W_{ad}$  is satisfied. (e) Simulation of deformation for the solid sample (top) and the MSA (bottom) at  $u = u_{cr}$  (stress unit: MPa). (f) Theoretical predictions of  $G_L$  versus crack length at various displacements for the MSA, with the red dashed line denoting  $W_{ad}$ . Positions marked by gray dash-dot lines correspond to locations labeled in the top right inset: A (the initial crack tip,  $X = X_0$ ), B ( $X = X_{min}$  where  $G_L = G_{L\_min}$ ), C (beam left), D ( $X = X_{max}$  where  $G_L = G_{L\_max}$ ), and E (beam right). Comparative analysis between experimental and predicted shear strength  $\tau$  (g) and effective adhesion energy  $\Gamma$  (h) of MSAs relative to solid samples.

both PMMA and PET, with PET characterized by a Young's modulus ( $E$ ) of 2950 MPa and Poisson's ratio ( $\nu$ ) of 0.43, and

PMMA with  $E$  of 2900 MPa and  $\nu$  of 0.4. We modeled the hollow backing structure as a Neo-Hookean material with a shear

modulus ( $\mu$ ) of 0.28 MPa. We set the bulk modulus at least 1000 times the shear modulus to account for incompressibility. As mentioned above, the PDMS adhesive layer ( $t \sim 0.08$  mm) is much thinner than the thinnest terminated film ( $t = 0.5$  mm) in this study. Additionally, PDMS and the hollow backing structure have similar shear moduli. Therefore, when computing the energy release rate, it is appropriate to ignore the ultra-thin PDMS adhesive layer in the geometry of the model. We introduced a seam crack with a length of  $C_0$  at the MSA-PMMA interface. We assumed plane strain conditions using CPE4RH elements. In the FEM modeling, we applied displacement control to the end of the PMMA plate while fixing the end of the PET film (Fig. 1a). We then obtained force-displacement curves from the simulation and calculated  $J$ -integral around the crack tip. We gradually increased the crack length by a finite value  $dC$ , and repeated the above process. We varied the crack length within a range greater than the spatial period  $\lambda$ . Finally, with energy release rate-displacement curves at different crack lengths, we processed the data to get energy release rate-crack length curves at different applied shear displacements. Mesh refinement, especially near the crack tip, was conducted through iterative refinement until simulation results converged.

### 3. Results

#### 3.1 The adhesion toughening arising from the crack trapping mechanism

In engineering applications like robotic grippers<sup>15,16,29</sup> and wall-climbing robotics,<sup>30,31</sup> structural adhesives usually experience shear load. In this study, we focus on lap shear experiments of MSAs in fracture-dominated conditions with no normal force applied to MSAs. As shown in Fig. 1a, we attached the MSA with a flexible PET backing layer to a rigid PMMA plate. We maintained the adhesive layer (a thin PDMS film cured from its precursor) unchanged throughout this study. We introduced an initial crack of  $C_0$  at the PDMS-PMMA interface, exceeding the sample height ( $H$ ) but much shorter than the sample length ( $L$ ) (Table S1, ESI†). We monotonically pulled the end of PMMA plate while fixing the end of PET film until the crack propagated through the entire interface. During the pulling, we recorded force-displacement curves (Fig. 1b). As expected, the MSA displays a smaller stiffness than the solid sample.

The adhesion enhancement of MSAs is achieved through the crack trapping mechanism as previously proposed,<sup>11,13,33,35,36</sup> which is briefly reformulated as follows. We establish a horizontal  $X$ -axis, with the origin ( $X = 0$ ) located at the center of the beam ahead of the crack (mark  $D$  in Fig. 1a). We assume the initial crack length is  $C_0$  with the tip located at  $X = X_0$  (mark  $A$  in Fig. 1a). When the crack propagates by a distance of  $\lambda$ , the crack tip reaches  $X = X_0 + \lambda$  (mark  $F$  in Fig. 1a). To maintain stable, equilibrium crack propagation, it is required that

$$G_L = W_{ad}, \text{ and } \frac{dG_L}{dc} < 0, \quad (1)$$

where  $c$  is the crack length,  $G_L$  is the energy release rate around the crack tip, and  $W_{ad}$  is the intrinsic work of adhesion.

For stable crack propagation, the averaged energy release rate is the same as  $W_{ad}$ .

However, for the MSA, at a fixed displacement  $u$ , due to its periodic beam structures, the local energy release rate  $G_L$  varies periodically in space (Fig. 1c):

$$G_L(c = C_0) = G_L(c = C_0 + \lambda). \quad (2)$$

To satisfy eqn (1), the applied displacement  $u$  needs to be varied with the crack length  $c$  non-monotonically during the crack propagation. However, in practice, the applied displacement  $u$  is usually monotonically increased, leading to unstable crack propagation.

As shown in Fig. 1c, at a small displacement ( $u = u_1$ ),  $G_L < W_{ad}$  at the initial crack tip prevents crack propagation. At a larger displacement ( $u = u_2$ ),  $G_L = W_{ad}$  is satisfied at the initial crack tip, yet crack propagation is hindered because  $\frac{dG_L}{dc} < 0$ . At an even larger displacement ( $u = u_3$ ), the crack front propagates unstably from the initial position (yellow circle) to the position indicated by the gray circle because  $G_L \geq W_{ad}$ . Afterwards, crack propagation stops because  $G_L < W_{ad}$  and  $\frac{dG_L}{dc} < 0$ . To overcome the crack trapping, a critical displacement ( $u = u_{cr}$ ) is required to achieve  $G_{L,min} = W_{ad}$  at both  $X = X_{min}$  and  $X = X_{min} + \lambda$ . When the crack propagates by a period from  $X = X_{min}$  to  $X = X_{min} + \lambda$ ,  $G_L > W_{ad}$  always holds true, resulting in unstable crack propagation. The total elastic energy stored in the MSAs before the critical displacement ( $u = u_{cr}$ ) is calculated as  $\int_{c=X_{min}}^{c=X_{min}+\lambda} G_L dc$ . Under practical monotonic loading in experiments, all the stored elastic energy is dissipated through unstable crack propagation. In addition to the energy required to separate the interface, the excess elastic energy compared to  $W_{ad}$  is fully dissipated through inelastic processes such as damping, damage, and viscoelasticity.<sup>11,13,33,35,36</sup>

Therefore, for our MSAs, we defined the effective adhesion energy ( $\overline{G_L}$ ) by averaging the reduction of elastic energy within one period ( $\lambda$ ) at  $u = u_{cr}$  (the blue shaded area in Fig. 1c), which is calculated as

$$\overline{G_L} = \frac{1}{\lambda} \int_{c=C_0}^{c=C_0+\lambda} G_L dc. \quad (3)$$

Similar definitions have been widely used to assess the toughening effect of periodically heterogeneous materials in previous studies.<sup>13,33,37,38</sup>

Based on the argument of the energy balance in fracture mechanics, we assume the work done by the external force is all dissipated by the formation of the new crack surface:

$$\int_{u=0}^{u=U_{debond}} F du = A_{eff} \Gamma_{exp}, \quad (4)$$

where  $A_{eff}$  is the effective adhesion area between the MSA and PMMA plate and  $\Gamma_{exp}$  is defined as the effective adhesion energy as shown in Fig. 1b.

Recall the definition of energy release rate  $G_L = -\frac{\partial U(u, c)}{\partial c}$ , where  $U$  is the elastic energy of the MSA per unit width and  $c$  is

the crack length. When the crack propagates through the entire interface, with the periodic assumption in eqn (3), we have

$$\Delta U = \int_{c=C_0}^{c=L} G_L dc = N\lambda\overline{G_L}, \quad (5)$$

where  $N$  is the number of periods and is defined as  $N = \frac{L - C_0}{\lambda}$ . Thus, we have

$$\Delta U = (L - C_0)\overline{G_L}, \quad (6)$$

which can be obtained using the integration of the blue shaded area in Fig. 1c.

Before the onset of crack propagation, the work done by the external force is stored as elastic energy in the MSA:

$$\int_{u=0}^{u=u_{\text{debond}}} F du = w\Delta U. \quad (7)$$

Thus, with eqn (4), (6) and (7), we can obtain

$$\frac{1}{A_{\text{eff}}} \int_{u=0}^{u=u_{\text{debond}}} F du = \Gamma_{\text{exp}} = \overline{G_L}, \quad (8)$$

which indicates the toughening effect of MSAs compared to solid samples that  $\Gamma_{\text{exp}} > W_{\text{ad}}$  for unstable crack propagation.

### 3.2 Experimental results and theoretical predictions

To confirm the crack trapping mechanism, we employ a hollow design featuring slender, tilted beams and a thick terminating film (the case with “ $b = 2.4$  mm” and “ $t = 2$  mm” in the first group of Table S1, ESI†) (Fig. 2a). As shown in Fig. S2a and Movie S1 (ESI†), the solid sample shows an initial crack opening upon the shear loading, followed by stable and fast propagation as the load increases. Eventually, adhesive failure occurs between the solid sample and PMMA plate. As shown in Fig. 2b and Movie S2 (ESI†), for the MSA, an initial crack opening is observed upon the shear loading. However, subsequent crack propagation stops on the left side of the beam. To enable further crack propagation, the loading needs to be further increased to advance the crack through the beam in an unstable manner. We observe periodic crack trapping and unstable crack propagation in experiments until the entire interface fails. Unless otherwise specified, adhesive failure was consistently observed between the PDMS adhesive layer and the PMMA plate in all tests.

We plot the crack propagation distance with time and find that crack propagation of the solid sample is much faster than that of the MSA (Fig. 2c). Additionally, the MSA displays stepwise increment of crack size, indicating crack trapping and unstable crack propagation as shown in Fig. 2b and Movie S2 (ESI†).

Both solid samples and MSAs exhibit reproducible force–displacement curves, with negligible dispersion across multiple samples (solid lines in Fig. 2d). We measure the intrinsic shear strength  $\tau_0$  (gray star) and work of adhesion  $W_{\text{ad}}$  (gray shaded area) from solid samples, which exhibit weak dependence on sample dimensions (Fig. S2b and c, ESI†). Similarly, we measure

the shear strength  $\tau_{\text{exp}}$  (blue star) and effective adhesion energy  $\Gamma_{\text{exp}}$  (blue shaded area) for MSAs.

We further conduct finite element analysis to quantitatively elucidate the adhesion toughening of MSAs. We truncate the predicted force–displacement curves at the critical displacement  $u = u_{\text{cr}}$  when  $G_{L_{\text{min}}} = W_{\text{ad}}$  is satisfied, which agree well with experimental results (dash-dot lines in Fig. 2d). Deformation profiles from finite element simulation also agree with experimental results (Fig. 2e). Next, we compute the  $G_L$ –crack length relationship from the simulations. For the solid sample,  $G_L$  remains nearly constant as a function of crack length provided that the initial crack is long enough (Fig. S2d, ESI†). At a critical displacement ( $u_{\text{cr}} = 1.12$  mm),  $G_L = W_{\text{ad}}$  and  $\frac{dG_L}{dc} = 0$  are satisfied, indicating the onset of stable crack propagation (Fig. S2d, ESI†). In contrast, for the MSA, the energy release rate  $G_L$  varies periodically with the crack length (Fig. 2f), reaching  $G_{L_{\text{min}}} = W_{\text{ad}}$  at the critical displacement ( $u_{\text{cr}} = 2.8$  mm). As explained in Fig. 1, unstable crack propagation occurs once  $G_{L_{\text{min}}} = W_{\text{ad}}$  is satisfied, which leads to adhesion toughening.

Experimental results reveal a shear strength of  $\tau_{\text{exp}} = 10.7$  kPa for MSAs, close to that of solid samples ( $\tau_0 = 10.2$  kPa) (Fig. 2g). The predicted shear strength of MSAs is  $\tau_{\text{pre}} = 13.6$  kPa, deviating by  $\sim 27\%$  from numerical predictions. We attribute such discrepancy to several factors: first,  $W_{\text{ad}} = 7.3$  J m<sup>−2</sup>, measured from solid samples, represents an averaged work of adhesion for rupturing the entire interface rather than the work of adhesion corresponding to crack initiation; second, our simulations assume a stable equilibrium state, neglecting all inelastic processes; third, by claiming  $\Gamma_{\text{exp}} = \overline{G_L}$ , we neglect the edge effects of the finite MSAs and viscoelastic dissipation; lastly, in the simulations, the initial crack doesn't propagate until  $G_{L_{\text{min}}} = W_{\text{ad}}$  is satisfied ( $u = u_{\text{cr}}$  in Fig. 1c), whereas in experiments, the crack propagates a little bit with the increase of displacement from  $u = u_2$  to  $u = u_{\text{cr}}$  (Fig. 1c).

Furthermore, the experimental effective adhesion energy of MSAs is  $\Gamma_{\text{exp}} = 13.3$  J m<sup>−2</sup>, nearly doubling that of solid samples ( $W_{\text{ad}} = 7.3$  J m<sup>−2</sup>) (Fig. 2h), showing the toughening effect. The predicted adhesion energy is  $\overline{G_L} = 10.6$  J m<sup>−2</sup> calculated with eqn (3) using the simulation results in Fig. 2f, close to our experimental results. The minor deviation from experimental results can be attributed to similar reasons discussed above.

### 3.3 Effects of the beam tilting angle $\theta$ on asymmetric adhesion

We next investigate the effects of beam tilting angle  $\theta$  on adhesion asymmetry while maintaining constant beam thickness  $b \cos(\theta)$  (group 1 listed in Table S1, ESI†). We pull the samples in two opposite directions (D1 and D2, as illustrated in Fig. 3a). With the pulling direction D1, tilted beams undergo buckling followed by stretching upon shear loading and simultaneously exhibit crack trapping behaviors (Fig. S3 and Movie S3, ESI†). Conversely, with the pulling direction D2, tilted beams immediately get stretched upon shear loading (Fig. 2b and Movie S2, ESI†). Consequently, MSAs exhibit

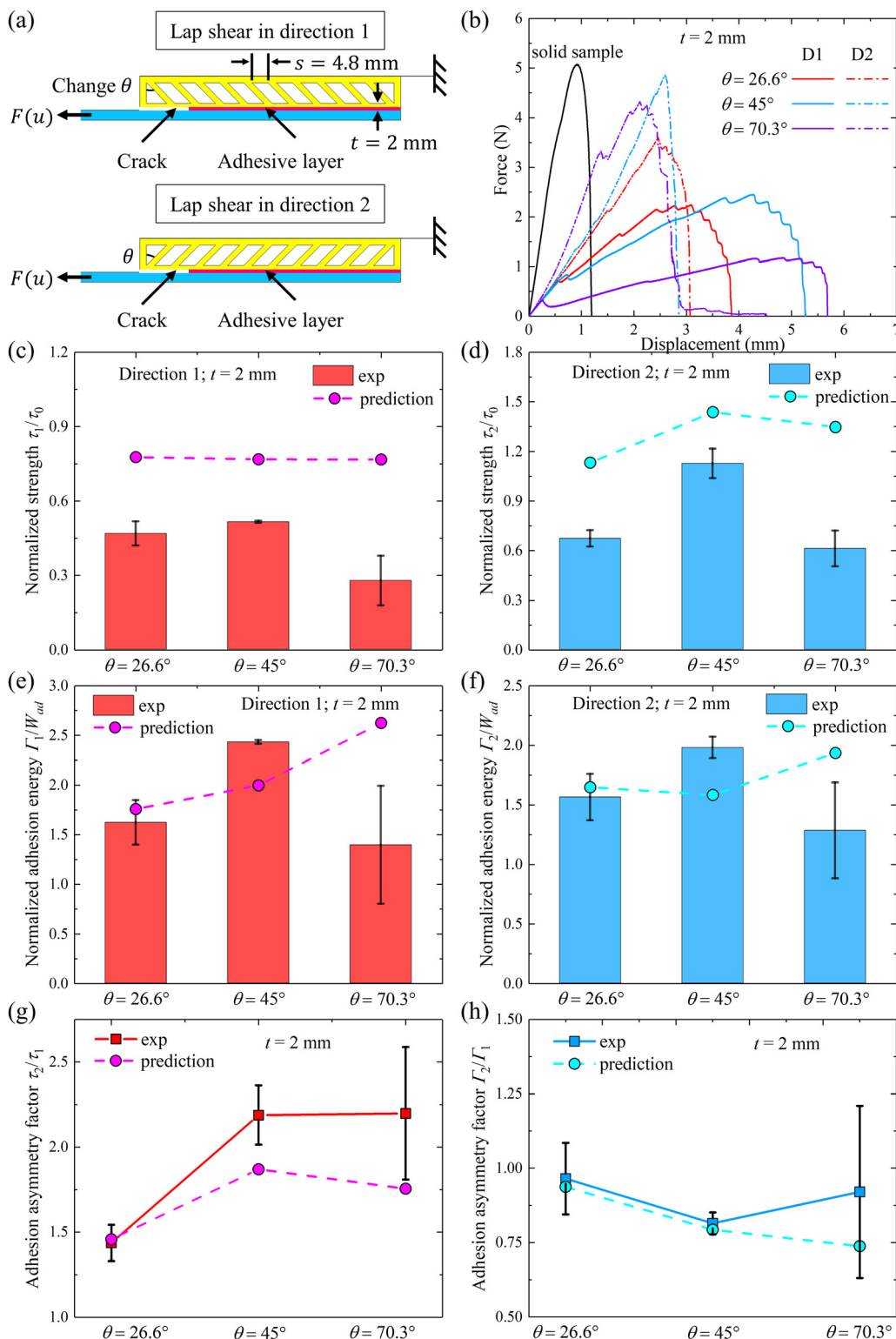


Fig. 3 Effects of the beam tilting angle ( $\theta$ ) on the asymmetric adhesion properties of MSAs with slender beams and a thick terminated film when the crack propagates unidirectionally along the predefined path. (a) Schematics showing the lap shear tests of MSAs with labeled geometric parameters for two opposite pulling directions (D1 and D2). (b) Effects of the beam tilting angle  $\theta$  on asymmetric force-displacement curves for two opposite pulling directions compared to the solid sample. Effects of the beam tilting angle  $\theta$  on the normalized shear strength (c)  $\tau_1/\tau_0$  and (d)  $\tau_2/\tau_0$  from experiments and theoretical predictions, respectively. Effects of the beam tilting angle  $\theta$  on the normalized effective adhesion energy (e)  $\Gamma_1/W_{ad}$  and (f)  $\Gamma_2/W_{ad}$  from experiments and theoretical predictions, respectively. Effects of the beam tilting angle  $\theta$  on the adhesion asymmetry factors (g)  $\tau_2/\tau_1$  and (h)  $\Gamma_2/\Gamma_1$  from experiments and theoretical predictions, respectively.

greater stiffness for the pulling direction D2 compared to D1 but are softer than solid samples (Fig. 3b). With the increase of  $\theta$ , the asymmetry in force–displacement curves for D1 and D2 pulling directions becomes more pronounced. In the experiments, the crack always propagates unidirectionally following the predefined path.

For the normalized shear strength  $\tau_i/\tau_0$  ( $i = 1$  or  $2$ ), our results show that  $\tau_1/\tau_0$  first remains nearly constant, slightly increasing

from  $\sim 0.47$  at  $\theta = 26.6^\circ$  to  $\sim 0.51$  at  $\theta = 45^\circ$ , and finally decreases significantly to  $\sim 0.28$  at  $\theta = 70.3^\circ$  (Fig. 3c). Meanwhile,  $\tau_2/\tau_0$  first increases from  $\sim 0.67$  at  $\theta = 26.6^\circ$  to  $\sim 1.1$  at  $\theta = 45^\circ$ , and then significantly decreases to  $\sim 0.61$  at  $\theta = 70.3^\circ$  (Fig. 3d). Our numerical predictions generally agree with experimental trends but are noticeably larger (colored circles in Fig. 3c and d).

For the normalized effective adhesion energy  $\Gamma_i/W_{ad}$  ( $i = 1$  or  $2$ ), our results show that  $\Gamma_1/W_{ad}$  first significantly increases from

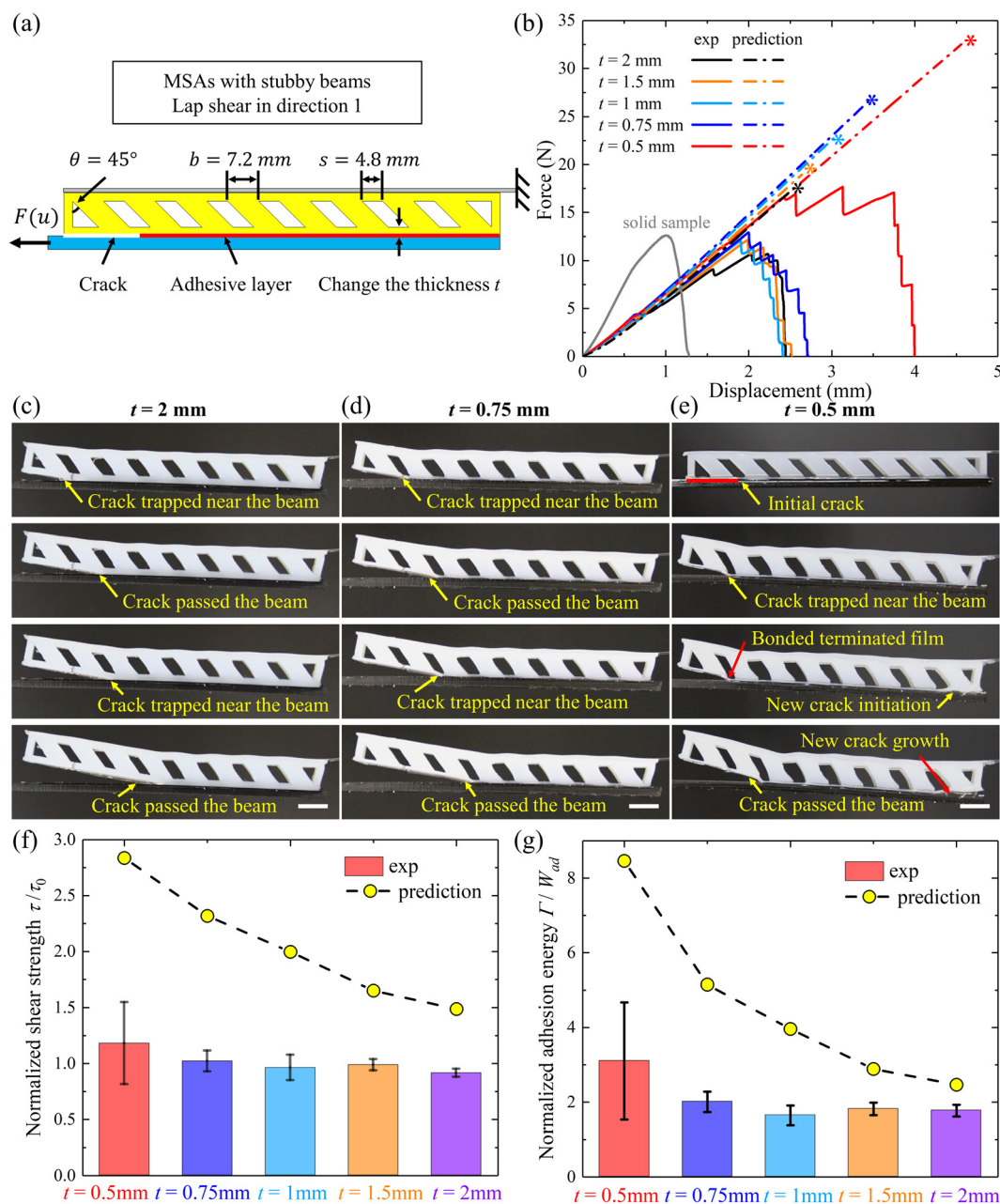
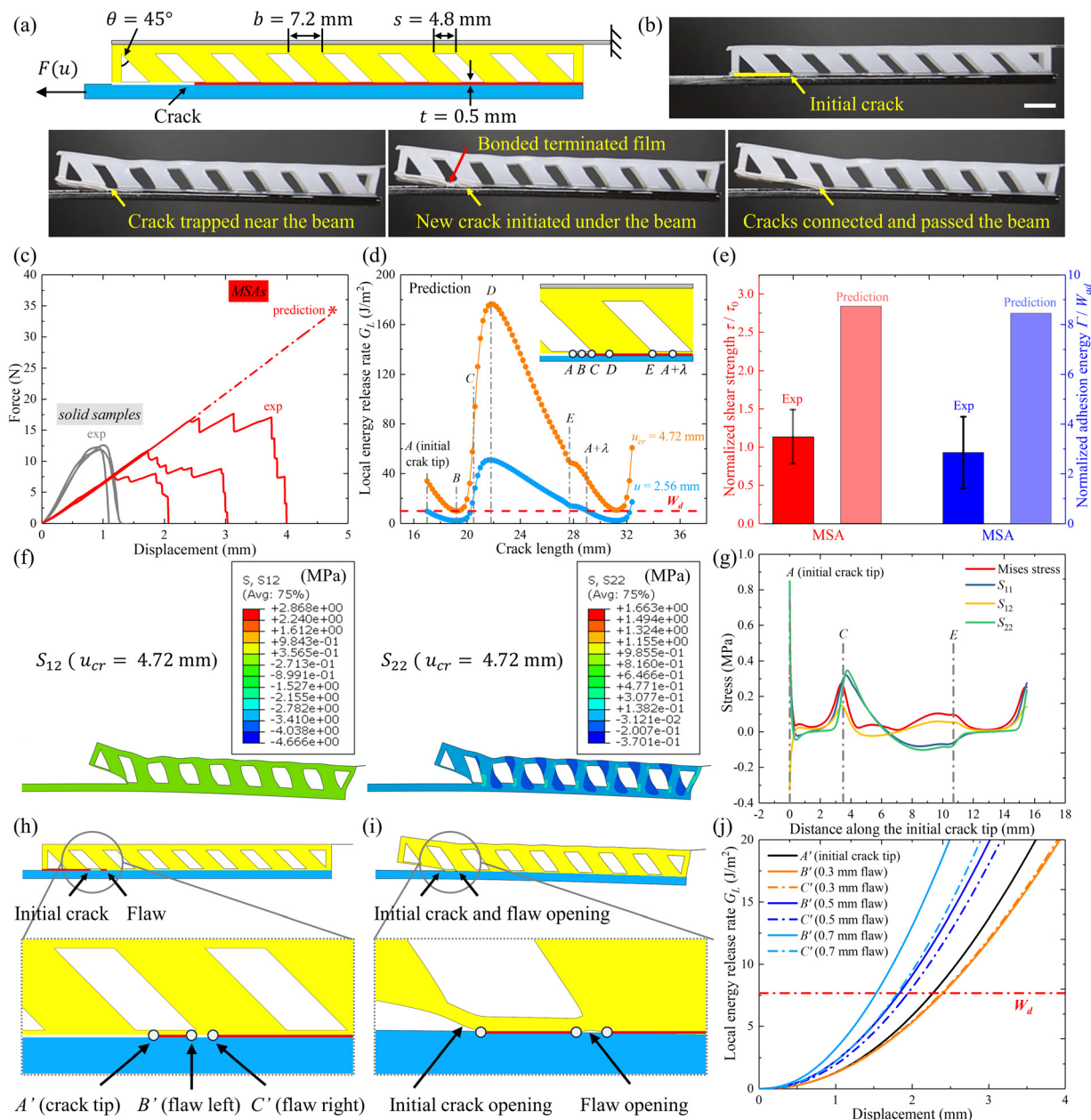


Fig. 4 Effects of the terminated film thickness ( $t$ ) on crack propagation dynamics and adhesion properties of MSAs with stubby beams from both experimental measurements and theoretical predictions. (a) Schematic showing the lap shear test and geometric parameters of MSAs with identical stubby beams but varied terminated film thickness ( $t$ ). (b) Effects of the terminated film thickness  $t$  on the force–displacement curves of MSAs compared to the solid sample. Representative images showing crack propagation dynamics of MSAs with a terminated film thickness of (c)  $t = 2$  mm, (d)  $t = 0.75$  mm, and (e)  $t = 0.5$  mm, respectively. All scale bars are 1 cm. Effects of the terminated film thickness  $t$  on (f) the normalized shear strength  $\tau/\tau_0$  and (g) the normalized adhesion energy  $\Gamma/W_{ad}$  of MSAs, respectively.

$\sim 1.6$  at  $\theta = 26.6^\circ$  to  $\sim 2.4$  at  $\theta = 45^\circ$ , and then significantly decreases to  $\sim 1.4$  at  $\theta = 70.3^\circ$  (Fig. 3e);  $\Gamma_2/W_{ad}$  first increases from  $\sim 1.6$  at  $\theta = 26.6^\circ$  to  $\sim 2.0$  at  $\theta = 45^\circ$ , and then decreases to  $\sim 1.3$  at  $\theta = 70.3^\circ$  (Fig. 3f). Our theoretical predictions generally agree with experimental results, with the exception for  $\theta = 70.3^\circ$  (colored circles in Fig. 3e and f).

Lastly, we define the adhesion asymmetry factors for strength ( $\tau_2/\tau_1$ ) and effective adhesion energy ( $\Gamma_2/\Gamma_1$ ), respectively.  $\tau_2/\tau_1$  first significantly increases from  $\sim 1.4$  at  $\theta = 26.6^\circ$  to  $\sim 2.2$  at  $\theta = 45^\circ$ , and then stays almost constant at  $\sim 2.2$  at  $\theta = 70.3^\circ$  (Fig. 3g). Meanwhile,  $\Gamma_2/\Gamma_1$  first slightly decreases from  $\sim 0.96$  at  $\theta = 26.6^\circ$  to  $\sim 0.81$  at  $\theta = 45^\circ$ , and then slightly increases to  $\sim 0.92$  at



**Fig. 5** New crack initiations along the interface lead to the discrepancy between experimental measurements and theoretical predictions for MSAs with a relatively thin terminated film. (a) Schematic showing the lap shear test and the geometric parameters of the MSA. (b) Representative images showing crack propagation dynamics, including new crack initiation alongside the propagation of the initial crack. Scale bar, 1 cm. (c) Experimental and numerically predicted force–displacement curves of MSAs compared to solid samples. (d) Numerically predicted variation of energy release rate  $G_L$  versus crack length, with the red dashed line representing  $W_{ad}$ . Various positions along the interface are marked in the top right inset and on the curves. (e) Comparison between experimental and numerically predicted  $\tau/\tau_0$  (left) and  $\Gamma/\Gamma_1$  (right), respectively. (f) Numerical calculations of the stress field of the MSA at the critical displacement of  $u_{cr} = 4.72$  mm. Left:  $S_{12}$  (unit: MPa). Right:  $S_{22}$  (unit: MPa). (g) Stress distribution along the interface near the initial crack. Marked positions are the same as those in (d). (h) Schematic showing the artificially introduced flaw (e.g., 0.7 mm) underneath the beam. (i) Deformed state of the initial crack and flaw at a displacement of  $u = 1.6$  mm. (j) Effects of the flaw size on the relationship between the energy release rate  $G_L$  and the applied displacement  $u$  at different positions. Marked positions are the same as those in (h).

$\theta = 70.3^\circ$  (Fig. 3h). Our numerical predictions mostly agree with our experimental findings, as indicated by the colored circles in Fig. 3g and h.

### 3.4 Effects of the terminated film thickness $t$ on adhesion properties

We next conduct a parametric study examining the influence of terminated film thickness ( $t$ ) on the adhesion properties. We design the second group of MSAs with identical stubby beams but varied film thickness  $t$  (see Fig. 4a and Table S1, ESI†) and test all the samples using identical experimental conditions. Our experimental results show that while the thickness  $t$  has minimal impact on the initial section of force–displacement curves, it significantly affects the latter portion (Fig. 4b). Such behavior stems from the dominance of tilted beams in carrying loads during elastic deformation, whereas the terminated film governs the energy release rate ( $G_L$ ) transferred to the crack tip during crack propagation, thus affecting the rupture point.<sup>13,33,35,36</sup>

Notably, when the terminated film thickness is decreased from  $t = 2$  mm to  $t = 0.75$  mm, the latter section of force–displacement curves shows a noticeable variation. However, further decreasing the thickness to  $t = 0.5$  mm leads to a dramatic increase in maximum shear force, accompanied by a pronounced dispersion of experimental measurements (shown in the next section; Fig. 5c).

Fig. 4c–e illustrate crack propagation dynamics of the MSAs with varied terminated film thickness. For a thick terminated film ( $t = 2$  mm), the crack propagates unidirectionally following the predefined path, exhibiting evident crack trapping behaviors (Fig. 4c). Conversely, for a thin terminated film ( $t = 0.5$  mm), we usually observe new crack initiations with a finite distance from the initial crack tip. Despite the presence of crack trapping behaviors, the crack propagation deviates from the predefined path (Fig. 4e). For an intermediate terminated film thickness ( $t = 0.75$  mm), the crack consistently propagates along the predefined path, displaying clear crack trapping behaviors (Fig. 4d). While random new crack initiations may still occur, they are not discernible in our recorded videos. See Movie S4 (ESI†) for details.

Consequently, as shown in Fig. 4f, the normalized shear strength  $\tau/\tau_0$  slightly increases with the decrease of  $t$ , ranging from  $\sim 0.91 \pm 0.04$  at  $t = 2$  mm to  $\sim 1.18 \pm 0.37$  at  $t = 0.5$  mm. Notably, for a thin terminated film ( $t = 0.5$  mm),  $\tau/\tau_0$  scatters greatly due to the randomly initiated new cracks. As shown in Fig. 4g, the normalized adhesion energy  $\Gamma/W_{\text{ad}}$  generally demonstrates a nonmonotonic change with the decrease of  $t$ , ranging from  $\sim 1.77 \pm 0.16$  for  $t = 2$  mm to  $\sim 3.1 \pm 1.57$  for  $t = 0.5$  mm. Similarly, for a thin terminated film ( $t = 0.5$  mm),  $\Gamma/W_{\text{ad}}$  scatters greatly due to the randomly initiated new cracks.

For a relatively large thickness ( $t = 2$  mm), the crack propagation follows the predefined path, and  $\tau/\tau_0$  and  $\Gamma/W_{\text{ad}}$  are close to the theoretical predictions based on the crack trapping mechanism (yellow circles in Fig. 4f and g). In contrast, for a relatively small thickness ( $t = 0.5$  mm), the propagation of the initial crack coexists with noticeable random new crack initiations, and  $\tau/\tau_0$  and  $\Gamma/W_{\text{ad}}$  are significantly smaller than the theoretical predictions (yellow circles in Fig. 4f and g).

For the intermediate thickness ranging from  $t = 1.5$  mm to  $t = 0.75$  mm, the theoretically predicted  $\tau/\tau_0$  and  $\Gamma/W_{\text{ad}}$  (Fig. 4f and g) deviate increasingly from experimental results. This deviation coincides with the gradual transition between the two distinct crack propagation modes mentioned above (Movie S4, ESI†). Clear experimental observation of this transition is challenging, attributed to the sample's opacity and the difficulty in discerning micro-scale crack initiations.

Similarly, for the third group of MSAs with identical slender beams (Table S1, ESI†), with the decrease of terminated film thickness ( $t$ ), the experimental results of adhesion properties deviate increasingly significantly from theoretical predictions (Text S1 and Fig. S4, ESI†).

### 3.5 New crack initiation reduces the enhancement of adhesion toughening

As discussed above, new crack initiation may be responsible for the difference between experimental results and theoretical predictions. While similar phenomena have been observed in the hollow structural adhesives with symmetric beams,<sup>13,33,35,36</sup> they have not been systematically studied. Herein, we systematically investigate the influence of new crack initiations on adhesion toughening, using MSAs featuring stubby beams and a thin terminating film as an example (“ $t = 0.5$  mm” cases in the second group of Table S1, ESI†; Fig. 5a). In experiments, the stochastic nature of new crack initiation results in varied crack propagation dynamics across different samples, and thus, we present another representative case in Fig. 5b and Movie S5 (ESI†), as a comparison with the results shown in Fig. 4e and Movie S4 (ESI†).

In experiments, we find significant scattering in the force–displacement curves of MSAs (Fig. 5c), and consequently significantly dispersed values of  $\tau/\tau_0$  (Fig. 5e, left) and  $\Gamma/W_{\text{ad}}$  (Fig. 5e, right), both of which are much smaller than the theoretically predicted values. Meanwhile, our simulations show that the energy release rate  $G_L$  changes more rapidly with the crack length (Fig. 5d) compared to that in Fig. 2f.

To investigate the possibility of new crack initiation, we first examine the stress field at the interface between the MSA and PMMA plate (Fig. 5f). We observe pronounced stress concentration near the left and right edges of the beam (marks  $C$  and  $E$  in the inset of Fig. 5d) by plotting the stress distribution against the distance from the initial crack tip along the interface (Fig. 5g), which is likely the cause of new crack initiation.

To quantitatively assess the impacts of inevitable flaws at the interface, we introduce a flaw along the interface beneath the left side of the beam (Fig. 5h). We repeat the simulation and compute the energy release rate at the initial crack tip ( $A'$ ), to the left of the flaw ( $B'$ ), and to the right of the flaw ( $C'$ ), respectively (Fig. 5h). Fig. 5i shows the deformation near the initial crack and the flaw (0.7 mm) with an applied displacement of  $u = 1.6$  mm. As shown in Fig. 5j, for a relatively small flaw (0.3 mm), the energy release rate  $G_L$  at the tips of the flaw is smaller than that at the initial crack tip. However, for a larger flaw size (0.5 mm or 0.7 mm),  $G_L$  at the tips of the flaw exceeds that at the initial crack tip, enabling new crack propagation before the propagation of the initial crack and thus decreasing

the measured adhesion energy. As the flaw size increases, the critical displacement  $u_{cr}$ , where  $G_L = W_{ad}$  is satisfied at the flaw tips, decreases.

Though our simulations have suggested the possibility of new crack initiations, our objective in the current study does not involve the theoretical prediction of adhesion toughening

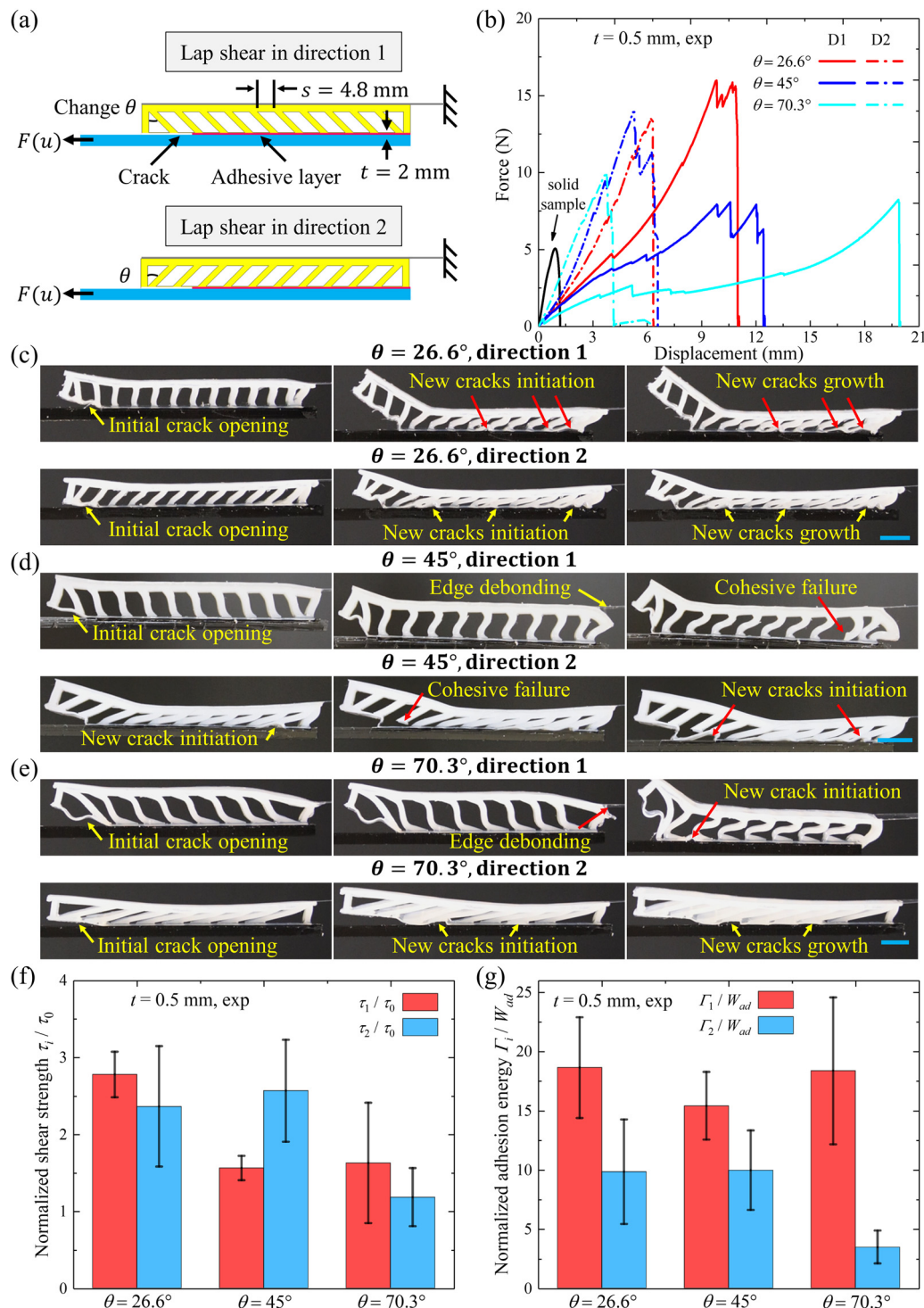


**Fig. 6** Optimization of adhesion toughening by varying the beam tilting angle ( $\theta$ ) of MSAs with a thin terminated film and slender beams. (a) Schematics showing the lap shear tests and geometric parameters of MSAs with two opposite pulling directions. (b) Effects of the beam tilting angle  $\theta$  on asymmetric force-displacement curves of MSAs for two opposite pulling directions. Representative images showing crack propagation dynamics for two opposite pulling directions with the beam tilting angle of (c)  $\theta = 26.6^\circ$ , (d)  $\theta = 45^\circ$ , and (e)  $\theta = 70.3^\circ$ , respectively. All scale bars are 1 cm. (f) Effects of the beam tilting angle  $\theta$  on  $\tau_1/\tau_0$  and  $\tau_2/\tau_0$ , respectively. (g) Effects of the beam tilting angle  $\theta$  on  $\Gamma_1/W_{ad}$  and  $\Gamma_2/W_{ad}$ , respectively.

in scenarios where new cracks initiate during the propagation of the initial crack, which can be extremely challenging.

### 3.6 Maximizing the adhesion toughening using MSAs with a thin terminated film

In this section, we experimentally explore the possibility of maximizing adhesion toughening using MSAs with slender beams and a thin terminated film ( $t = 0.5$  mm) (group 4 listed in Table S1, ESI†; Fig. 6a). We vary the beam tilting angle  $\theta$  while maintaining constant beam thickness  $b \cos(\theta)$ , and perform lap shear tests in two opposite pulling directions, respectively.

Our experimental results show increased asymmetry in force–displacement curves for the two opposite pulling directions with the increase of  $\theta$  (Fig. 6b). We present representative images and movies illustrating crack propagation dynamics for different designs of MSAs (Fig. 6c–e). At  $\theta = 26.6^\circ$ , new crack initiations occur along the interface during the propagation of the initial crack for both pulling directions (Fig. 6c and Movie S6, ESI†). At  $\theta = 45^\circ$ , both edge debonding from the PET film and cohesive failure within the hollow backing occur during the propagation of the initial crack for the D1 pulling direction; for the D2 pulling direction, cohesive failure and new crack initiations occur along the interface during the propagation of the initial crack (Fig. 6d and Movie S7, ESI†). At  $\theta = 70.3^\circ$ , both edge debonding from PET film and new crack initiations occur during the propagation of the initial crack for the D1 pulling direction; for the D2 pulling direction, new cracks initiate during the propagation of the initial crack (Fig. 6e and Movie S8, ESI†).

Consequently,  $\tau_1/\tau_0$  first decreases significantly from  $\sim 2.8$  at  $\theta = 26.6^\circ$  to  $\sim 1.6$  at  $\theta = 45^\circ$ , and then remains nearly constant at  $\sim 1.6$  at  $\theta = 70.3^\circ$ ; but  $\tau_2/\tau_0$  first remains almost unchanged from  $\sim 2.4$  at  $\theta = 26.6^\circ$  to  $\sim 2.6$  at  $\theta = 45^\circ$ , and then decreases to  $\sim 1.2$  at  $\theta = 70.3^\circ$  (Fig. 6f). Similarly,  $\Gamma_1/W_{ad}$  first decreases from  $\sim 18.6$  at  $\theta = 26.6^\circ$  to  $\sim 15.4$  at  $\theta = 45^\circ$ , and then increases to  $\sim 18.4$  at  $\theta = 70.3^\circ$ ;  $\Gamma_2/W_{ad}$  first remains almost constant from  $\sim 9.8$  at  $\theta = 26.6^\circ$  to  $\sim 10.0$  at  $\theta = 45^\circ$ , and then decreases to  $\sim 3.5$  at  $\theta = 70.3^\circ$  (Fig. 6g). Finally, the adhesion asymmetry factor  $\tau_2/\tau_1$  significantly increases from  $\sim 0.85$  at  $\theta = 26.6^\circ$  to  $\sim 1.6$  at  $\theta = 45^\circ$ , and then decreases to  $\sim 0.73$  at  $\theta = 70.3^\circ$  (Fig. S5a, ESI†). Similarly,  $\Gamma_2/\Gamma_1$  slightly increases from  $\sim 0.53$  at  $\theta = 26.6^\circ$  to  $\sim 0.65$  at  $\theta = 45^\circ$ , and then significantly decreases to  $\sim 0.19$  at  $\theta = 70.3^\circ$  (Fig. S5b, ESI†).

## 4. Discussion

In the following, we discuss several critical points that require further in-depth investigations.

Our theoretical predictions of adhesion toughening, based on the crack trapping mechanism,<sup>11,13,33,35,36</sup> agree well with experimental results when the crack propagates unidirectionally following a predefined path for a relatively thick terminated film. However, with the decrease of the terminated film thickness, the measured adhesion energy of MSAs deviates significantly from theoretical predictions, which is attributed to new

crack initiations based on experimental observations and numerical simulations. However, the transition between the two distinct crack propagation modes remains unclear and may indicate the involvement of the fracto-adhesive length scale, which characterizes the thickness-dependent adhesion properties, as systematically investigated in a previous study on the lap shear of soft hydrogels.<sup>39</sup> Note that currently, the length scales governing the fracture and adhesion of discrete metamaterials are yet to be explored,<sup>9,12,40,41</sup> which calls for more comprehensive theoretical and experimental investigations.

Recently, stretchable and low-hysteresis composites comprising hard and soft phases have been developed to enhance both the fracture toughness and fatigue resistance.<sup>34,42,43</sup> While the stress deconcentration mechanism has been widely used to elucidate toughening effects, the periodically varied relationship between energy release rate *versus* crack length based on the crack trapping mechanism provides an alternative way to predict the fracture and fatigue enhancement.

In this study, lap shear tests were conducted without normal force applied to MSAs. We want to point out that lap shear tests under displacement control (using two rigid fixtures) are rare in practical applications but prevalent in lab tests,<sup>39,44–46</sup> which can lead to significant artifacts for thick structural adhesives (Fig. S6a and b, ESI†). For both solid samples and MSAs, the maximum shear force is much higher in displacement-control mode than in zero normal force-control mode when the displacement along the thickness direction is fixed (Fig. S6c and d, ESI†). Consequently, solid samples exhibit appreciable increases in shear strength and adhesion energy in displacement-control mode (Fig. S6e and f, ESI†). For MSAs, both shear strength and effective adhesion energy show significant increases in displacement-control testing mode (Fig. S6e and f, ESI†). The reason is as follows: with displacement-control mode, the stress normal to the applied shear force increases significantly for MSAs due to beam bending, compared to solid samples. This significantly increases the friction between MSAs and PMMA substrate, resulting in mixed-mode fracture. These findings highlight the importance of carefully selecting the lap shear conditions for testing thick structural adhesives.<sup>44</sup>

Finally, we envision that there are ample opportunities for further exploration of MSAs. For example, stimuli-responsive materials can be used to fabricate either the thick backing or the adhesive layer for stimuli-responsive MSAs targeted at responsive and switchable applications.<sup>5</sup> Besides, designing the backing structures of MSAs to better conform to rough or curved surfaces may enable strong and reversible adhesion, addressing the well-known challenge of conventional pressure sensitive adhesives.<sup>47,48</sup> Furthermore, exploring MSAs for achieving strong and reversible adhesion in wet and underwater conditions is also important for biomedical applications and ocean explorations.<sup>49,50</sup>

## 5. Conclusions

In summary, we have achieved adhesion toughening and asymmetry in the lap shear of MSAs using asymmetric and

thick hollow backings. By combining theoretical, numerical, and experimental investigations, we identify the crack trapping as the toughening mechanism, which leads to unstable crack propagation under practical monotonic loading and thus dissipates more energy. For MSAs with a relatively thick terminated film, the experimental results agree well with theoretical predictions based on the crack trapping mechanism when the crack propagates unidirectionally along the predefined path. However, for MSAs with a relatively thin terminated film, the experimental results deviate significantly from theoretical predictions based on the crack trapping mechanism. We attribute this discrepancy to new crack initiations, which are observed experimentally and elaborated through numerical simulations. Additionally, we explore adhesion asymmetry by varying the beam tilting angle ( $\theta$ ). Notably, for MSAs with  $t = 0.5$  mm and  $\theta = 26.6^\circ$ , we achieve a maximum effective adhesion energy being  $\sim 18.6$  times that of solid samples. For MSAs with  $t = 0.5$  mm and  $\theta = 70.3^\circ$ , we achieve a maximum adhesion energy asymmetry factor of  $\Gamma_1/\Gamma_2 \sim 5.3$ . Our study provides useful insights for designing metamaterial structural adhesives for engineering applications such as robotic grippers, wall-climbing robotics, and wearable devices that require reversible and switchable adhesion.

## Author contributions

C. L. and S. C. conceived the study and designed the overall experiments. Q. G. provided suggestions on the interpretation of experimental results and numerical simulations. R. C. helped with 3D-printing the molds. C. L. and S. C. wrote the manuscript with input from all authors. All authors read and approved the final article.

## Data availability

The authors confirm that the data supporting the findings of this study are available within the article and its ESI.†

## Conflicts of interest

The authors declare they have no competing interests.

## Acknowledgements

The authors acknowledge support from the US Army Research Office through grant no. W911NF-20-2-0182.

## References

- 1 C. Creton, *MRS Bull.*, 2003, **28**, 434–439.
- 2 M. M. Feldstein, E. E. Dormidontova and A. R. Khokhlov, *Prog. Polym. Sci.*, 2015, **42**, 79–153.
- 3 S. Nam and D. Mooney, *Chem. Rev.*, 2021, **121**, 11336–11384.
- 4 J. Yang, R. Bai, B. Chen and Z. Suo, *Adv. Funct. Mater.*, 2020, **30**, 1901693.
- 5 N. D. Belloch, H. J. Yarbrough and K. A. Mirica, *Chem. Sci.*, 2021, **12**, 15183–15205.
- 6 Z. Liu and F. Yan, *Adv. Sci.*, 2022, **9**, 2200264.
- 7 A. B. Croll, N. Hosseini and M. D. Bartlett, *Adv. Mater. Technol.*, 2019, **4**, 1900193.
- 8 X. Zhao, X. Chen, H. Yuk, S. Lin, X. Liu and G. Parada, *Chem. Rev.*, 2021, **121**, 4309–4372.
- 9 D. Hwang, C. Lee, X. Yang, J. M. Pérez-González, J. Finnegan, B. Lee, E. J. Markvicka, R. Long and M. D. Bartlett, *Nat. Mater.*, 2023, **22**, 1030–1038.
- 10 Q. Li, W. Liu, C. Yang, P. Rao, P. Lv, H. Duan and W. Hong, *J. Mech. Phys. Solids*, 2022, **169**, 105053.
- 11 S. Xia, L. Ponson, G. Ravichandran and K. Bhattacharya, *Phys. Rev. Lett.*, 2012, **108**, 196101.
- 12 A. E. Athanasiadis, M. A. Dias and M. K. Budzik, *Extreme Mech. Lett.*, 2021, **48**, 101411.
- 13 N. J. Glassmaker, A. Jagota, C.-Y. Hui, W. L. Noderer and M. K. Chaudhury, *Proc. Natl. Acad. Sci. U. S. A.*, 2007, **104**, 10786–10791.
- 14 R. Zhao, S. Lin, H. Yuk and X. Zhao, *Soft Matter*, 2018, **14**, 2515–2525.
- 15 W. Ruotolo, D. Brouwer and M. R. Cutkosky, *Sci. Rob.*, 2021, **6**, eabi9773.
- 16 X. Zhang, Y. Wang, Z. Tian, M. Samri, K. Moh, R. M. McMeeking, R. Hensel and E. Arzt, *Sci. Adv.*, 2022, **8**, eadd4768.
- 17 A. Ghareeb and A. Elbanna, *J. Appl. Mech.*, 2019, **86**, 071005.
- 18 Q. Li, X. Wan, Z. Xu, Y. He, Q. Xue and C. Yang, *Extreme Mech. Lett.*, 2024, **67**, 102128.
- 19 Y. He, X. Wan, Y. Chen and C. Yang, *J. Mech. Phys. Solids*, 2021, **155**, 104570.
- 20 Y. Gao, X. Jiang, P. Wang, Y. Zhong and T. Lu, *Extreme Mech. Lett.*, 2023, **61**, 102016.
- 21 H. Zhu, T. Yin, X. Hu, B. Liu, H. Yu, Z. Chen, S. Qu and W. Yang, *J. Mech. Phys. Solids*, 2023, **175**, 105304.
- 22 S. Xia, L. Ponson, G. Ravichandran and K. Bhattacharya, *J. Mech. Phys. Solids*, 2015, **83**, 88–103.
- 23 S. Xia, L. Ponson, G. Ravichandran and K. Bhattacharya, *J. Mech. Phys. Solids*, 2013, **61**, 838–851.
- 24 Y. Xie, Y. Wu, Z. Wei, J. Lin and J. Qian, *Eur. J. Mech. A: Solids*, 2024, **103**, 105159.
- 25 D.-G. Hwang, K. Trent and M. D. Bartlett, *ACS Appl. Mater. Interfaces*, 2018, **10**, 6747–6754.
- 26 B. W. Townsend, D. C. Ohanehi, D. A. Dillard, S. R. Austin, F. Salmon and D. R. Gagnon, *Int. J. Adhes. Adhes.*, 2011, **31**, 639–649.
- 27 B. W. Townsend, D. C. Ohanehi, D. A. Dillard, S. R. Austin, F. Salmon and D. R. Gagnon, *Int. J. Adhes. Adhes.*, 2011, **31**, 650–659.
- 28 E. Bull, J. Cholaky and S. Kuhlman, *Durability of Building and Construction Sealants and Adhesives*, ASTM International, 2015, vol. 5, pp. 297–327.
- 29 S. Song, D.-M. Drotlef, C. Majidi and M. Sitti, *Proc. Natl. Acad. Sci. U. S. A.*, 2017, **114**, E4344–E4353.
- 30 G. Gu, J. Zou, R. Zhao, X. Zhao and X. Zhu, *Sci. Rob.*, 2018, **3**, eaat2874.

- 31 J. Huang, Y. Liu, Y. Yang, Z. Zhou, J. Mao, T. Wu, J. Liu, Q. Cai, C. Peng, Y. Xu, B. Zeng, W. Luo, G. Chen, C. Yuan and L. Dai, *Sci. Rob.*, 2021, **6**, eabe1858.
- 32 H. Yao, G. D. Rocca, P. Guduru and H. Gao, *J. R. Soc., Interface*, 2008, **5**, 723–733.
- 33 L. Shen, C.-Y. Hui and A. Jagota, *J. Appl. Phys.*, 2008, **104**, 123506.
- 34 Z. Wang, C. Xiang, X. Yao, P. Le Floch, J. Mendez and Z. Suo, *Proc. Natl. Acad. Sci. U. S. A.*, 2019, **116**, 5967–5972.
- 35 Z. He, N. M. Moyle, C.-Y. Hui, B. Levrard and A. Jagota, *Tribol. Lett.*, 2017, **65**, 1–8.
- 36 W. Noderer, L. Shen, S. Vajpayee, N. Glassmaker, A. Jagota and C.-Y. Hui, *Proc. R. Soc. A*, 2007, **463**, 2631–2654.
- 37 P. Fratzl, H. S. Gupta, F. D. Fischer and O. Kolednik, *Adv. Mater.*, 2007, **19**, 2657–2661.
- 38 M. Hossain, C.-J. Hsueh, B. Bourdin and K. Bhattacharya, *J. Mech. Phys. Solids*, 2014, **71**, 15–32.
- 39 Y. Wang, X. Yang, G. Nian and Z. Suo, *J. Mech. Phys. Solids*, 2020, **143**, 103988.
- 40 S. Fulco, M. K. Budzik, E. D. Bain and K. T. Turner, *Extreme Mech. Lett.*, 2022, **57**, 101912.
- 41 A. J. D. Shaikeea, H. Cui, M. O'Masta, X. R. Zheng and V. S. Deshpande, *Nat. Mater.*, 2022, **21**, 297–304.
- 42 C. Xiang, Z. Wang, C. Yang, X. Yao, Y. Wang and Z. Suo, *Mater. Today*, 2020, **34**, 7–16.
- 43 C. Li, H. Yang, Z. Suo and J. Tang, *J. Mech. Phys. Solids*, 2020, **134**, 103751.
- 44 S. A. Suresh, A. Hajj-Ahmad, E. W. Hawkes and M. R. Cutkosky, *J. R. Soc., Interface*, 2021, **18**, 20200730.
- 45 H. Yuk, C. E. Varela, C. S. Nabzdyk, X. Mao, R. F. Padera, E. T. Roche and X. Zhao, *Nature*, 2019, **575**, 169–174.
- 46 Y. Wang, T. Yin and Z. Suo, *J. Mech. Phys. Solids*, 2021, **150**, 104348.
- 47 C. Linghu, Y. Liu, Y. Y. Tan, J. H. M. Sing, Y. Tang, A. Zhou, X. Wang, D. Li, H. Gao and K. J. Hsia, *Proc. Natl. Acad. Sci. U. S. A.*, 2023, **120**, e2221049120.
- 48 Z. Wang, Y. Dong, R. Annapooranan, C. Li, R. Chambers and S. Cai, *Appl. Mater. Today*, 2024, **38**, 102189.
- 49 C. Lee, H. Shi, J. Jung, B. Zheng, K. Wang, R. Tutika, R. Long, B. P. Lee, G. X. Gu and M. D. Bartlett, *Cell Rep. Phys. Sci.*, 2023, **4**, 101597.
- 50 S. T. Frey, A. T. Haque, R. Tutika, E. V. Krotz, C. Lee, C. B. Haverkamp, E. J. Markvicka and M. D. Bartlett, *Sci. Adv.*, 2022, **8**, eabq1905.